Monthly Notices
of the
ROYAL ASTRONOMICAL SOCIETY

MNRAS **449,** 1454–1469 (2015) doi:10.1093/mnras/stv314

The Gigaparsec WiggleZ simulations: characterizing scale-dependant bias and associated systematics in growth of structure measurements

Gregory B. Poole,[1,2★] Chris Blake,[1] Felipe A. Marín,[1] Chris Power,[3] Simon J. Mutch,[2] Darren J. Croton,[1] Matthew Colless,[4] Warrick Couch,[5] Michael J. Drinkwater[6] and Karl Glazebrook[1]

[1]*Centre for Astrophysics and Supercomputing, Swinburne University of Technology, PO Box 218, Hawthorn, VIC 3122, Australia*
[2]*School of Physics, University of Melbourne, Parksville, VIC 3010, Australia*
[3]*ICRAR, University of Western Australia, 35 Stirling Highway, Crawley, WA 6009, Australia*
[4]*Research School of Astronomy and Astrophysics, Australian National University, Weston Creek, ACT 2600, Australia*
[5]*Australian Astronomical Observatory, PO Box 915, North Ryde, NSW 1670, Australia*
[6]*School of Mathematics and Physics, University of Queensland, Brisbane, QLD 4072, Australia*

Accepted 2015 February 12. Received 2015 February 11; in original form 2014 June 20

ABSTRACT

We present the Gigaparsec WiggleZ simulation suite and use this resource to characterize galaxy bias and its scale dependence for a range of redshifts and halo masses in a standard Λ cold dark matter cosmology. Under the ansatz that bias converges to a scale-independent form at large scales, we develop an eight-parameter phenomenological model which fully expresses the mass and redshift dependence of bias and its scale dependence in real- or redshift space. This is then used to illustrate how scale-dependent bias can systematically skew measurements of the growth rate of cosmic structure obtained from redshift-space distortion measurements. When data is fit only to scales $k_{\rm max} \leq 0.1\ [h^{-1}\,{\rm Mpc}]^{-1}$, we find that these effects are significant only for large biases ($b \gtrsim 3$) at large redshifts ($z \gtrsim 1$). However, when smaller scales are incorporated ($k_{\rm max} \lesssim 0.2\ [h^{-1}\,{\rm Mpc}]^{-1}$) to increase measurement precision, the combination of reduced statistical uncertainties and increased scale-dependent bias can result in highly significant systematics for most large haloes across all redshifts. We identify several new interesting aspects of bias, including a significant large-scale bias boost for small haloes at low redshifts due to substructure effects ($\sim$20 per cent for Milky Way-like systems) and a nearly redshift-independent halo mass (corresponding to a redshift-space bias of $\sim$1.5) for which halo bias has little or no scale dependence on scales greater than 3 [h^{-1}Mpc]. This suggests an optimal strategy of targeting bias $\sim$1.5 systems for clustering studies which are dominated more by systematic uncertainties in how observed halo (or galaxy) distributions map to their underlying mass distribution than by observational statistical precision, such as cosmological measurements of neutrino masses. Code for generating our fitting formula is publicly available at http://gbpoole.github.io/Poole_2014a_code/.

Key words: surveys – cosmological parameters – cosmology: theory – large-scale structure of Universe.

1 INTRODUCTION

Maps of the distribution of galaxies across enormous cosmic volumes – as determined from galaxy redshift surveys – have become extremely rich resources for a variety of powerful examinations of cosmological models. These include (but are certainly not limited to) precise standard ruler measurements of the cosmic expansion history using harmonic features induced by 'baryon acoustic oscillations' (BAOs) in the Universe's matter density field and measurements of the growth rate of cosmic structure as probed by the imprints of the cosmic peculiar velocity field on redshift-derived (i.e. redshift-space) distributions of galaxies. Our ability to perform these and other cosmological examinations using redshift surveys is based upon our ability to connect observed galaxy distributions to our highly developed and robust models of the distribution of matter in the early Universe, its evolution with redshift and the dependence of both on background cosmology. Of course, the success of this

★ E-mail: gpoole@unimelb.edu.au

endeavour rests completely on our ability to relate observed galaxy distributions to their underlying matter distributions; a relationship generally referred to as 'galaxy bias'. However, it has long been understood observationally that galaxy bias has a complicated dependency on galaxy luminosity, colour and morphology (Loveday et al. 1995; Hermit et al. 1996) with modern studies still continuing to refine this understanding (e.g. Norberg et al. 2001; Zehavi et al. 2005; Ross, Brunner & Myers 2007; Swanson et al. 2008; Cresswell & Percival 2009, see Baugh 2013 for a review).

In this paper, we seek to characterize this relationship. We aim to build a phenomenological parametrization of halo bias and its scale dependence across a range of masses and redshifts which we can use to ascertain when and to what degree scale-dependant bias becomes important for observational measurements of the growth rate of cosmological structure. Several ancillary outcomes will also result including a correction to large-scale bias estimates for substructure effects or for systems exhibiting strong scale-dependant bias, useful for other studies intimately linked to the redshift evolution of bias.

As with most aspects of large-scale structure, a great deal of theoretical insight can be obtained through excursion set analyses. The earliest successful theory of this type was that of Kaiser (1984, subsequently extended by Bardeen et al. 1986) who illustrated how the two-point clustering statistics of collapsed cosmological objects becomes enhanced if associated with early overdensities in the cosmological matter field. The first model to build explicitly upon the popular framework of Press & Schechter (1974) and its extensions (EPS) was that of Mo & White (1996, MW) which was subsequently confronted by the numerical investigation of Jing (1998) who identified significant discrepancies in this model's treatment of lower mass systems. These discrepancies were traced to incorrect assumptions about the form of the halo mass function in MW by Sheth & Tormen (1999) who were able to build a successful analytic model constructed from mass functions calibrated by numerical simulations, thus establishing an intimate link between the mass-dependent clustering bias of a halo population and its associated mass function. This was soon followed by Sheth, Mo & Tormen (2001, SMT) who added an account of the dynamics of ellipsoidal collapse to the traditional EPS approach through the adoption of a mass dependence for the spherical collapse overdensity, leading to significant improvements in the excursion set results for both mass functions and the mass dependence of large-scale bias (although, see Borzyszkowski, Ludlow & Porciani 2014, for a recent challenge to this interpretation).

Generally, two approaches to the analysis of halo bias exist: Eulerian approaches (which dominate the literature) focus on the contemporaneous relationship of halo and matter clustering and Lagrangian approaches which relate the evolving clustering of haloes to their *initial* linear-regime matter field. Interesting challenges to the conclusions of Eulerian studies have emerged from Lagrangian studies. For example, Porciani, Catelan & Lacey (1999) utilized simulations to show that the low-mass bias modifications of Jing (1998, mentioned above) to the analytic model of MW reflects conditions embedded in the initial state of the simulations, and not exclusively subsequent non-linear processes. Such findings motivate a careful examination of traditional excursion set descriptions of halo formation; a conclusion echoed by Jing (1999) and subsequently built upon by several studies including Ludlow & Porciani (2011) and Elia, Ludlow & Porciani (2012).

While analytic progress continues to be made (e.g. Ma et al. 2011, who employ a non-Markovian extension and a stochastic collapse barrier within the framework of traditional EPS approaches to obtain improved mass function and bias models), the work of SMT makes it clear that treatment of the detailed structure of collapsing cosmological fields are important to obtaining accurate estimates of volume-averaged clustering statistics. As a result, most significant progress has been driven of late by improved calibrations of analytic models using *N*-body simulations (e.g. Seljak & Warren 2004; Tinker et al. 2005). This effort has culminated in Tinker et al. (2010, TRK) who examine a more generalized form of the SMT model and perform a careful numerical calibration of its parameters. Recent studies have validated the TRK model (Papageorgiou et al. 2012; see Basilakos & Plionis 2001; Basilakos, Plionis & Ragone-Figueroa 2008) which we will use as our main comparison for the large-scale bias calculations which anchor the scale-dependent bias analysis in this work.

While large-scale galaxy bias has received a great deal of study, relatively few inquiries have been made into its scale dependence. Early examinations (e.g. Sheth & Lemson 1999; Casas-Miranda et al. 2002; Zehavi et al. 2004; Seo & Eisenstein 2005) have discussed some general expectations and presented evidence of scale-dependant bias in observed data sets but the work of Tinker et al. (2005) is the first to present a general model. Subsequently, in their clustering analysis of the 2dF Galaxy Redshift Survey, Cole et al. (2005) introduced the 'Q-model': a phenomenological Fourier-space model which has subsequently found applications in the analysis of Sloan luminous red galaxies (LRGs) (e.g. Padmanabhan et al. 2007). Employing arguments based on the halo model, other Fourier-space accounts of scale-dependent bias include the model of Schulz & White (2006, subsequently extended by Huff et al. 2007) and Smith, Scoccimarro & Sheth (2007) who clearly illustrate the existence of scale-dependent bias and a dependence on halo mass and galaxy type. Furthermore, Pollack, Smith & Porciani (2014) have recently explored scale-dependent bias within standard perturbation theory finding that the non-linear processes giving rise to such effects are not sufficiently described in popular second-order local Eulerian schemes. Lastly, Paranjape et al. (2013) have shown how to identify and remove scale-dependant bias effects using simulated halo catalogues resulting in large-scale biases which are in good agreement to those of TRK.

Observationally, an important additional complication arises. Positions for very large ensembles of galaxies are generally not determined through direct distance measurements but are rather inferred from redshifts. Distributions measured in this way are said to be constructed in 'redshift space' and the presence of peculiar velocities imprinted upon the background Hubble-flow by accelerations from local density gradients is known to induce significant bias effects in this space. The classic treatment by Kaiser (1987, K87 henceforth) predicts that coherent bulk flows on large scales induce a 'Kaiser boost': a significant increase in clustering bias over that which would be inferred in real space due to halo assembly effects alone. On large scales, this model has been validated by numerical simulations (e.g. Montesano, Sánchez & Phleps 2010) but on small scales – where incoherent motions such as those giving rise to the 'Fingers of God' effect can lead to a *suppression* of bias – significant scale-dependence to these redshift-space effects has been identified (e.g. Seljak 2001).

The primary consequence of scale-dependent bias is that it introduces a source of systematic uncertainty to cosmology constraints at a level which is now important for ongoing and future surveys. While several investigations have found that the consequences for constraints based on the scale of the BAO peak should not be significant (e.g. Eisenstein, Seo & White 2007; Angulo et al. 2008; Crocce & Scoccimarro 2008; Smith, Scoccimarro & Sheth 2008, a conclusion supported by our investigations), there is concern that

constraints sensitive to the full *shape* of scale-dependent clustering statistics (such as power spectra or correlation functions) will be more susceptible, particularly when pushed to smaller scales. Two notable such cases include measurements of neutrino masses from the cosmological power spectrum (e.g. Riemer-Sørensen et al. 2012) and measurements of the growth rate of cosmic structure (e.g. Blake et al. 2011a) which we focus on in this study.

Beyond the issue of systematic bias, several interesting physical processes can lead to scale-dependent bias providing new opportunities for the study of other physics. These include the induction of scale-dependent bias from departures from non-Gaussianity in the early universe (Dalal et al. 2008; Slosar et al. 2008; Taruya, Koyama & Matsubara 2008) or from subtle environmental effects induced by the physics of galaxy formation (Coles & Erdogdu 2007; Barkana & Loeb 2011). Firmly establishing an accurate and robust theory in the absence of these effects will be essential for their search in observational data sets.

In this work, we take a distinctly different approach from past studies, performing a straightforward phenomenological characterization of Eulerian bias in configuration space. Surprisingly little theoretical investigation of scale-dependent bias within this framework has been performed in the recent literature despite the fact that it is the space in which most observational analysis is performed. As noted by Huff et al. (2007, also see Guzik, Bernstein & Smith 2007), configuration space offers an important advantage over Fourier space: a lower amplitude of scale-dependent bias. Interpreted within the framework of the halo model, they note that this is due to the fact that most scale-dependent bias is a product of the different scales on which matter and galactic haloes transition from the one-halo regime to the two-halo regime. This occurs on relatively small scales as far as most cosmological studies are concerned, thus isolating its effects in configuration space. In Fourier space, such broad-spectrum features become spread across a wider range of scales transferring signal from the small scales on which the phenomena occurs, to larger scales where most of the clustering signal resides.

We use the Gigaparsec WiggleZ (GiggleZ) simulation suite for this study. GiggleZ was constructed to support the science program of the WiggleZ Dark Energy Survey (Drinkwater et al. 2010) – a large redshift survey of UV-selected galaxies conducted with the multiobject AAOmega fibre spectrograph at the 3.9-m Australian Astronomical Telescope – and has been used in several WiggleZ-related publications to date (e.g. Blake et al. 2011b; Riemer-Sørensen et al. 2012; Contreras et al. 2013; Marín et al. 2013; Blake, James & Poole 2014). We take this opportunity to present details related to the construction of the GiggleZ simulation program and subsequently present a simple and direct model of the mass and redshift dependence of both large-scale and scale-dependent bias of dark matter haloes. We examine for the first time the effects of substructure on models of galaxy bias of this form, finding significant (∼20 per cent) effects on low-bias systems at low redshift. We then use this model to build upon previous studies of systematic biases in growth of structure measurements (Jennings, Baugh & Pascoli 2011; Okumura & Jing 2011; Contreras et al. 2013), calculating the potential magnitude of systematic errors induced in the absence of corrections for scale-dependent bias effects.

In Section 2 we present the GiggleZ simulation suite; the simulations involved, our approach to initializing, running and analysing them, and the results of a convergence study run to determine the optimal integration properties of our adopted simulation code. In Section 3 we present our scale-dependent bias model, stepping through the justifications for each of our chosen parametrizations. In Section 4 we present the consequences of scale-dependent bias for growth of structure measurements. Lastly, we summarize and discuss our conclusions in Section 5.

Our choice of fiducial cosmology throughout will be a standard spatially flat *WMAP*-5 Λ cold dark matter (ΛCDM) cosmology (Komatsu et al. 2009): $(\Omega_\Lambda, \Omega_M, \Omega_b, h, \sigma_8, n) = (0.727, 0.273, 0.0456, 0.705, 0.812, 0.960)$.

2 SIMULATIONS

The GiggleZ simulation suite consists of five simulations: a large GiggleZ-main run consisting of 2160^3 particles distributed in a periodic box 1 $[h^{-1}\,\mathrm{Gpc}]$ on-a-side, and four simulations of an identical 125 $[h^{-1}\,\mathrm{Mpc}]$ on-a-side control volume spanning a factor of 512 in mass resolution with snapshot temporal resolutions as fine as 15 Myr. The basic specifications for these five runs are listed in Table 1. The large scale of the GiggleZ-main simulation was motivated by the unprecedented combination of large volume and low halo mass of the low-bias UV-selected galaxies targeted by WiggleZ. Such observational programmes present a demanding challenge for theoretical support of clustering studies, leading us to create (at the time) one of the highest-resolution gigaparsec-scale cosmological simulations available, comparable to modern simulation programmes such as the Multidark BigBolshoi simulation (Prada et al. 2012). The control-volume simulations were designed to conduct systematic studies of the resolution requirements for semi-analytic galaxy formation studies. In this paper, we focus on the GiggleZ-main simulation only. A companion paper will present the control-volume simulations in detail where they are used to present our method of merger tree construction and their convergence properties.

We have run our simulations with GADGET-2 (Springel 2005), a Tree-Particle Mesh code well suited to large distributed memory systems. We have modified the publicly available version to conserve RAM in dark matter only simulations by removing all support for hydrodynamics, 'FLEXSTEP' time stepping and variable particle masses (along with all associated memory allocations).

Table 1. Box sizes (L), particle counts (N_p), particle mass (m_p), number of snapshots (n_{snap}), approximate snapshot temporal resolution (Δt) and gravitational softening length (ϵ) for the GiggleZ simulations.

Simulation	$L\ [h^{-1}\,\mathrm{Mpc}]$	N_p	$m_p\ [10^9\,\mathrm{M}_\odot\,h^{-1}]$	n_{snap}	Δt [Myr]	$\epsilon\ [h^{-1}\,\mathrm{kpc}]$
GiggleZ-main	1000	2160^3	7.52	100	115	9.3
GiggleZ-LR	125	135^3	60.13	931	15	18.5
GiggleZ-NR	125	270^3	7.52	931	15	9.3
GiggleZ-MR	125	540^3	0.95	467	30	4.6
GiggleZ-HR	125	1080^3	0.12	235	60	2.3

All simulations were run on the Green Machine at Swinburne University, with the largest run consuming all the resources of 124 nodes, each housing dual quad core Intel Clovertown 64 bit processors (for a total of 992) with 16 GB of RAM.

2.1 Initial Conditions

To initialize our simulations, we use the Parallel *N*-body Initial Conditions (PaNICs) code developed at Swinburne for this project. PaNICs follows the approach of Bertschinger (2001) to construct a displacement field which, when applied to a uniform distribution of particles, yields a distribution with our desired power spectrum. This power spectrum was generated using CAMB (Lewis, Challinor & Lasenby 2000) with our standard spatially flat *WMAP*-5 ΛCDM cosmology given above. This power spectrum was normalized for a starting redshift $z_{\rm init} = 49$ for the GiggleZ-main run and $z_{\rm init} = 499$ for the control-volume simulations. These starting redshifts ensure that initial particle displacements are smaller than the grid cell size of the displacement field for all simulations, a condition advocated by Lukić et al. (2007). This high starting redshift may introduce some numerical noise for the lower resolution control-volume runs affecting detailed halo structure, but should have a negligible effect on the mass accretion histories which will be the main focus of their use. This was verified for the GiggleZ-NR mass resolution during our convergence testing in which we performed a run with $z_{\rm init} = 49$ and found no significant effect on the simulation's halo power spectrum or mass function.

For the GiggleZ-main simulation, the displacement field was computed on a 4320^3 grid while the control-volume simulations used a common displacement field computed on a 2160^3 grid. Uniform distributions in all cases were computed from integral periodic tilings of a 135^3 glass configuration (see White 1994, for more details) generated using GADGET.

Particle velocities were computed from the PaNICs displacement field using the Zeldovich approximation (Zel'Dovich 1970; Buchert 1992). Higher order corrections to this calculation (e.g. Scoccimarro 1998; Crocce, Pueblas & Scoccimarro 2006) could not be implemented in a timely fashion for this project, but will certainly be incorporated in future projects.

2.2 Halo finding

The majority of the analysis in this study will utilize the bound dark matter haloes which emerge from our simulations. To extract these structures we use the well tested code SUBFIND of Springel et al. (2001). This code first starts by finding friends-of-friends (FoF) structures for which we use the standard linking length criterion of $0.2\bar{d}$ (where $\bar{d} = L/\sqrt[3]{N_{\rm p}}$ denotes the mean interparticle spacing of the simulation). It subsequently identifies bound substructures within these FoF groups as locally overdense collections of particles, removing unbound particles through an unbinding procedure.

This procedure leads to two classes of halo: FoF groups and substructure haloes. In the work which follows, we perform our analyses on both classes of halo separately. Since FoF groups are more closely related to the overdensity peaks forming the basis of Extended Press–Schechter analyses, results derived from study of these objects should form a better comparison to models developed within that framework. However, observed galaxy populations are more closely related to our substructure haloes and results derived from analyses of this class of halo should be more straightforwardly related to observed galaxy distributions. Later in Section 3.4 we will find that there are interesting differences between the bias properties of the two.

2.3 Convergence tests

Being principally responsible for the accuracy and run time of our simulations, we carefully considered the settings of two GADGET parameters in particular when setting up our calculations: the gravitational softening (ϵ; we will express this in units of $\bar{d}$ henceforth) and the dimensionless parameter controlling the accuracy of the time step criterion (η; referred to as ErrTolIntAccuracy in the GADGET manual).

We ran a grid of $(L, N) = (250\ [h^{-1}\,{\rm Mpc}],\ 540^3)$ simulations (i.e. the same mass resolution as the GiggleZ-main and GiggleZ-NR run), varying combinations of these parameters over the ranges $\epsilon = 0.005\bar{d}$–$0.08\bar{d}$ and $\eta = 0.005$–0.04. Since our primary science interests in WiggleZ involve studies of L^* galaxy formation and clustering on 100 $[h^{-1}\,{\rm Mpc}]$ scales, we seek convergence based on the substructure halo mass function and substructure halo power spectrum of haloes in the range ${\rm M} > 10^{12}\ [h^{-1}\,{\rm M}_\odot]$.

The results are presented in Fig. 1. Expected trends are realized: larger softenings in particular have a strong impact on small scales (i.e. low mass and high k). Furthermore, we find that the power spectrum is a more stringent condition in these tests than the mass function. When $P(k)$ is converged, the mass function is converged. Using the power spectrum at $z = 0$ as our metric of fitness, we can immediately rule out softenings $\epsilon > 0.04\bar{d}$ by demanding that deviations from our fiducial $P(k)$ remain less than 5 per cent over the range $k = 0.1$–$1\ [h^{-1}\,{\rm Mpc}]^{-1}$.

There is a degeneracy in these tests between ϵ and η: moderate increases in ϵ can be compensated for by decreasing η. Reducing η has a significant impact on the run time of the simulation however, placing practical constraints on how far it can be lowered. Taken in combination, we use these constraints to settle upon the combination $(\epsilon, \eta) = (0.02\bar{d}, 0.01)$ for all runs in this project. From these experiments, we expect the mass function to be accurate to ∼2 per cent on M^* scales. We expect the power spectrum to be accurate to ∼2 per cent over the range $k = [0.1, 1]\ [h^{-1}\,{\rm Mpc}]^{-1}$.

2.4 Halo groupings

For this study, we are interested in the mass and redshift dependence of halo clustering properties. To facilitate our analysis, we have assembled a number of 'groupings' of both our FoF and substructure haloes for a set of seven redshifts from $z = 0$ to ∼1.2 in steps of ${\rm d}z \sim 0.2$. In each case we have rank-ordered the structures by their maximum circular velocities (denoted $V_{\rm max}$) and selected contiguous groupings of $n_i(z_i, V_{{\rm max},\,i})$ systems (yielding grouping number densities of n_i per $\left[h^{-1}\,{\rm Gpc}\right]^3$) for each 'i'th grouping. This is done such that $V_{{\rm max},\,i}$ are median values for their respective groupings, starting at 150 km s^{-1} for $i = 0$ and extending upwards in steps of 10 km s^{-1} until we run out of massive haloes (at a value of $V_{{\rm max},\,i}$ which declines with redshift). We use $V_{\rm max}$ as our metric of halo mass to render our results less sensitive to peculiarities of our chosen halo finder and to increase reproducibility. Furthermore, subhalo abundance matching has suggested that $V_{\rm max}$ may more directly parametrize the stellar mass of galaxies (Reddick et al. 2013), potentially improving the degree to which our $V_{\rm max}$-selected subhalo groupings represent the clustering characteristics of stellar-mass selected galaxy samples. See Fig. 2 for an illustration of the relationship between $V_{\rm max}$ and $M_{\rm vir}$.

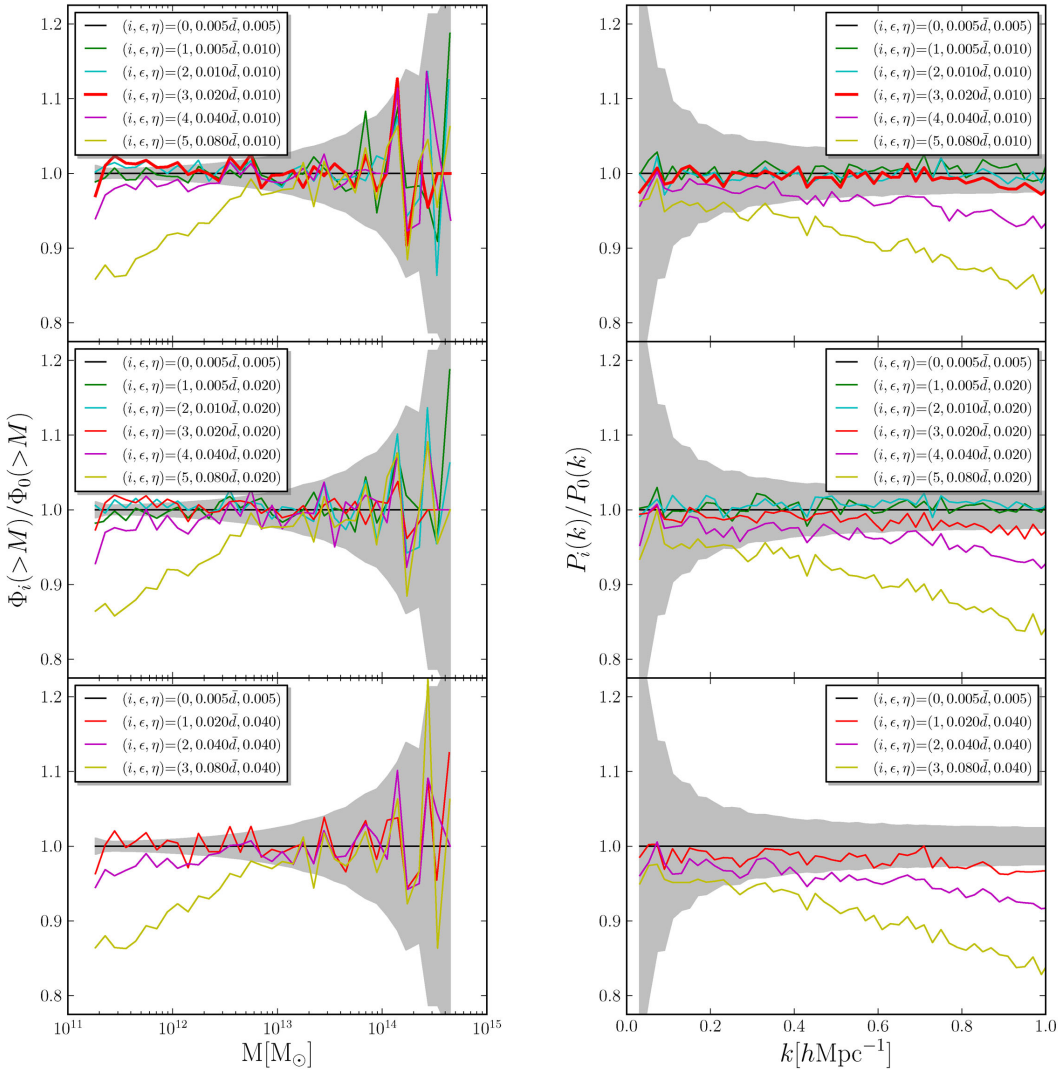

Figure 1. A plot comparing the effects of variations in gravitational softening parameter (ϵ) and time step integration accuracy (η) on the mass function (Φ_i; left) and power spectrum of haloes more massive than 10^{12} M$_\odot$ (P_i; right) of a (L, N) = (250 [h^{-1} Mpc], 540^3) simulation (i.e. the same mass resolution as the GiggleZ-main and GiggleZ-NR runs). In each case, we normalize the mass function and power spectrum to the case (ϵ, η) = (0.005$\bar{d}$, 0.005). Based on these results, we selected (ϵ, η) = (0.02$\bar{d}$, 0.01) for all GiggleZ simulations (where $\bar{d}$ is the mean interparticle spacing of the simulation). Runs with $\epsilon = 0.02\bar{d}$ are labelled in red with the $\eta = 0.01$ case additionally highlighted with a thick line (top panels). Grey shaded regions indicate the magnitude of the Poisson statistical uncertainty of the (ϵ, η) = (0.005$\bar{d}$, 0.005) case used as reference in all cases.

We set n_i for each grouping to yield correlation functions of roughly equivalent signal to noise despite the growth of structure moderated by the linear growth factor (denoted by D and given by $D = \delta(z)/\delta(0)$, where $\delta(z)$ is the evolving matter density contrast) and the mass-dependent bias which we estimate using the TRK model[1] (denoted by b_{TRK}). This approach has the added benefit of naturally reducing our bin size as mass and redshift increase, adapting to regimes where halo densities are low and clustering properties are rapidly evolving. More specifically, we choose groupings for which $b_{\mathrm{TRK}}(V_{\mathrm{max},\,i},\ z_i) = 1$ to have $n_i = 10^5$ haloes at $z = 0.6$ and scale n_i for other cases by $1/(b_{\mathrm{TRK}}D)$. The resulting values of n_i used for this study are illustrated in Fig. 2.

[1] Throughout this paper, we will convert the overdensity parametrizing this model to an effective V_{max} assuming standard Navarro, Frenk & White (1997) scaling properties and the mass-concentration relation of Muñoz-Cuartas et al. (2011).

To add redshift-space distortion effects to our catalogues we assume a flat-sky approximation, taking the positions of each halo grouping and adding a 1D displacement in the x-direction (δx) given by

$$\delta x = \frac{v_x h}{a(z)H(z)}, \tag{1}$$

where v_x is the x-component of the physical centre-of-mass velocity of the halo, $a(z)$ is the cosmological expansion factor and $H(z)$ is the redshift-dependant Hubble parameter.

3 ANALYSIS

For the analysis presented in this paper, we will use the two-point correlation function as our measure of clustering strength and its scale dependence. The method of Landy & Szalay (1993) is used throughout and is applied to all of the halo groupings described in Section 2.4 as well as to randomly sampled subsets of 10^6

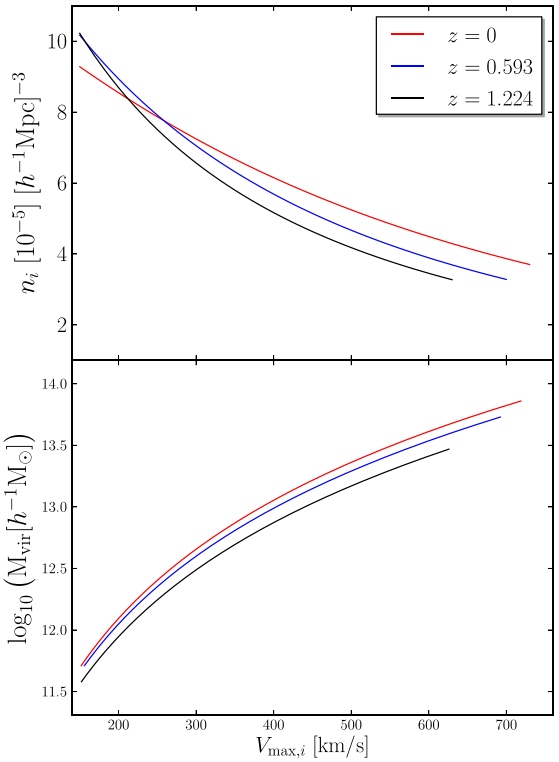

Figure 2. A plot presenting the number densities (n_i) adopted for the halo 'groupings' and the relationship between $V_{\rm max}$ and $M_{\rm vir}$ used for all analysis in this work. Three redshifts evenly spanning the range of this study ($z \lesssim 1.2$) are depicted. Number densities are chosen such that they scale inversely with large-scale bias (as estimated from the model of TRK) and the linear growth factor (i.e. $n_i \propto 1/(b_{\rm TRK}D)$) normalized such that $n_i(z_i = 0.6, b_{\rm TRK} = 1) = 10^5$ $[(h\,\mathrm{Gpc}^{-1})^3]$.

particles from each relevant snapshot of our simulations. This method requires a large number of randomly distributed points and we use 250 000 points for halo analysis and 5×10^6 for matter field analysis, ensuring that there are at least five times more random points than data points in all cases.

Examples of our computed correlation functions are presented in Fig. 3 where we show results at three redshifts evenly spanning the range of our study ($z = 0$, 0.593 and 1.224) for distributions of matter and for FoF halo groupings of three masses ($V_{\rm max} =$ 150, 300 and 450 [km s^{-1}]) in the GiggleZ-main simulation. Expected trends of increasing clustering amplitude with halo mass and increased redshift-space clustering (particularly on scales less than $\sim$2 [h^{-1} Mpc] where 'halo exclusion' effects become significant) are apparent.

3.1 Computing scale-dependent bias and motivating its general form

Throughout the analysis which follows, we will focus on three correlation function ratios which capture separate contributions to halo bias and its scale dependence. These ratios will be between the redshift-space halo correlation function and the real-space halo correlation function ($\mathcal{R}_{\rm z}$, said to express the redshift-space – or Kaiser, after the model of K87 – 'boost' effects on total bias), the ratio of the real-space halo correlation function to the real-space dark matter correlation function ($\mathcal{R}_{\rm h}$, said to express the real-space halo bias) and the ratio of the redshift-space halo correlation function to the real-space dark matter correlation function ($\mathcal{R}_{\rm t}$, said to express the total or redshift-space bias). Throughout this work we will refer to these ratios in a general form as $\mathcal{R}_x$ where $x =$ 'z','h' or 't' denoting the Kaiser boost, halo or redshift-space bias ratios, respectively. Conceptually, $\mathcal{R}_{\rm t} = \mathcal{R}_{\rm h} \times \mathcal{R}_{\rm z}$, although we fit to each ratio individually and do not enforce this relation.

In all cases, $\mathcal{R}_x(s)$ profiles and uncertainties are computed from the median and (potentially asymmetric) distribution of 216 jackknife subsamples evaluated using a regular 6^3 grid. This choice for the number of jackknife regions was motivated by the work presented in Contreras et al. (2013) where we found that results are insensitive to the number of regions used for the regimes studied here. Furthermore, we concentrate only on scales larger than 3 [h^{-1} Mpc] for two reasons: we find that the behaviour of $\mathcal{R}_x(s)$ on scales less than this is complicated (with a character similar to that presented in fig. 4 of Zehavi et al. 2004) and difficult to parametrize and because it is on scales less than this where the morphology–density relation of observed galaxy populations becomes significant (Haines et al. 2009; Hansen et al. 2009; von der Linden et al. 2010; Lu et al. 2012; Rasmussen et al. 2012; Wetzel, Tinker & Conroy 2012; Bahé et al. 2013), greatly complicating the use of these scales for realistic galaxy populations.

Examples of each ratio for cases spanning the range of redshift and halo mass addressed by this study are shown in Fig. 4 (for all plots henceforth, the same colour scheme is used: green to represent real-space halo bias, red to represent Kaiser boost effects and black to represent total redshift-space bias). Several general trends are immediately obvious from this plot. At large scales, the limited volume of our simulation results in a rapid increase in the variance of each $\mathcal{R}_x$ profile as scales begin to exceed 20–30 [h^{-1} Mpc]. Within these admittedly large uncertainties, there is little evidence of scale-dependent bias effects beyond these scales, as we expect from the results of previous studies. At smaller scales where our simulation is adequate for quantifying $\mathcal{R}_x(s)$, we see clear evidence of scale dependence increasing in magnitude with halo mass and redshift for $\mathcal{R}_{\rm h}$ and $\mathcal{R}_{\rm t}$ while trends are more mild and less discernible for $\mathcal{R}_{\rm z}$. Furthermore, in some regimes we find that $\mathcal{R}_x$ can be enhanced on small scales relative to large scales (generally the case for $\mathcal{R}_{\rm h}$ and $\mathcal{R}_{\rm t}$) or suppressed on small scales.

Therefore, taking as an ansatz that $\mathcal{R}_x$ converges to a constant value at large scales (although, see Angulo et al. 2014, for evidence of slight scale-dependent effects on scales >140 [h^{-1} Mpc], albeit at a level insignificant to this study), this figure motivates us to assume the following form for $\mathcal{R}_x$:

$$\mathcal{R}_x = b_x^2(1 + \mathcal{S}\,(s/s_x)^{-\eta}),$$
$$\text{where} \quad \mathcal{S} = \pm 1. \tag{2}$$

This is a four-parameter model (applicable on scales $s > 3\,[h^{-1}\,\mathrm{Mpc}]$) where b_x quantifies the large-scale bias amplitude, η sets the slope of $\mathcal{R}_x$ on small scales, s_x is effectively a measurement of the amplitude of scale-dependent effects (in the same way that r_0 parametrizes clustering amplitude when correlation functions take the form $\xi = (\frac{r}{r_0})^\gamma$, particularly for a fixed value of η as we will ultimately adopt below) and $\mathcal{S}$ sets whether bias is suppressed by scale-dependent effects on small scales (i.e. the case $\mathcal{S} = -1$) or enhanced on small scales (i.e. the case $\mathcal{S} = +1$).

3.2 The mass dependence of scale-dependent bias

In Fig. 5 we show the results of fitting the model introduced in equation (2) to each scale-dependence ratio, for all of our halo

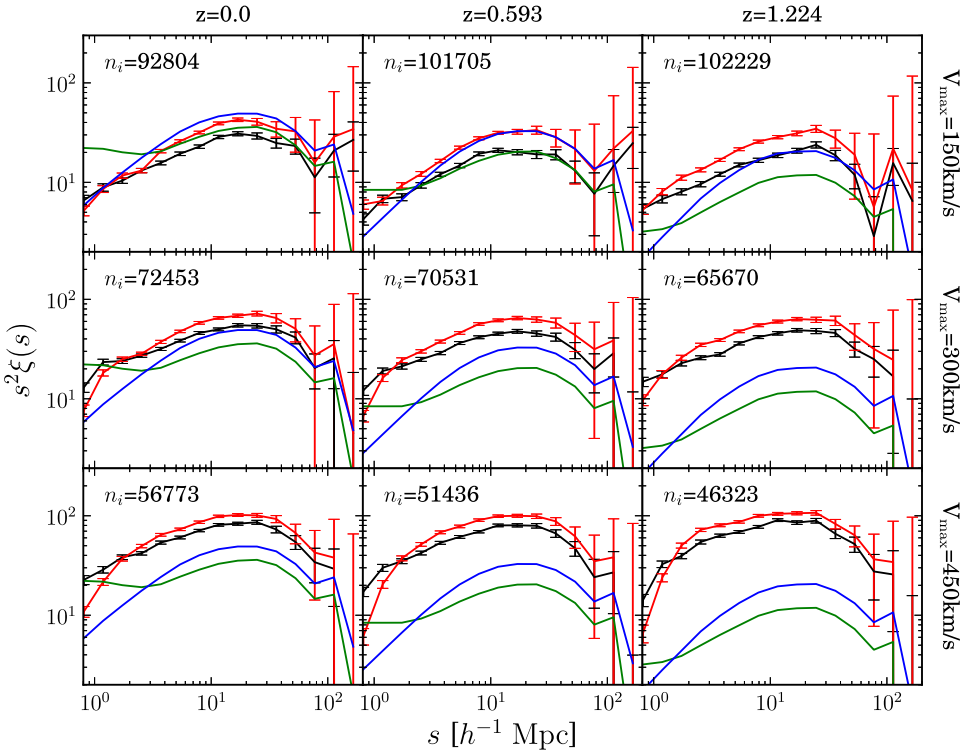

Figure 3. Two-point correlation functions ($\xi(s)$; plotted as $s^2\xi(s)$ with an extra factor of s^2 to increase figure clarity) for the total matter and for populations of dark matter haloes at three halo masses and three redshifts. Green and blue lines denote $\xi(s)$ in real- and redshift space for the dark matter particles at each redshift, respectively. Black and red lines with error bars denote $\xi(s)$ in real- and redshift space for the dark matter haloes, respectively. In all cases, the number haloes involved in the represented FoF halo groupings (n_i) are given. Uncertainties are computed from jackknife subsamples using a regular 6^3 grid. Values across the top denote the redshift represented by each column while values along the right indicate the halo mass (expressed in terms of maximum halo circular velocity, V_{max}) represented by each row.

groupings at three redshifts spanning the range of our study. These preliminary illustrative fits – which at this point are meant only to motivate the parametrization which follows – are constructed using a simple χ^2-minimization approach.

When allowing η to vary freely between values of 0 and 3, we find very little discernible trend for η with V_{max} and very noisy trends for s_x with V_{max} for all three bias types. This suggests that the four-parameter model of equation (2) is underconstrained by these data sets. However, when we fix η to a value of 1, clear trends in $s_x(V_{max})$ emerge for all cases, as illustrated in Fig. 5. Fixing η in this way results in a minimal reduction in the quality of fit, as shown in the bottom panels of this figure where we compare the χ^2 obtained allowing η to vary ($n_{DoF} = 5$) to those obtained when we fix η to a value of 1 ($n_{DoF} = 6$). This value of η was chosen as a compromise in the range of best-fitting values. While the results of fits change in detail when other fixed values of η are chosen, little change results to the quality of fit or to the conclusions of our study.

For the large-scale bias parameters (b_x, illustrated in the top panels of Fig. 5), expected trends are apparent with real-space and redshift-space halo bias increasing with both mass and redshift. They follow each other with an offset which decreases with mass but is relatively constant with redshift. This offset is due to Kaiser boost contributions which we see decline with mass, converging towards a value of 1 (i.e. no contribution to redshift-space bias from peculiar velocities) as masses increase. This trend is remarkably constant with redshift as well.

As mentioned above, when we fix η to a value of 1, s_x effectively quantifies the amplitude of scale-dependent bias effects. For this choice of η, a value of $s_x = 1$ [h^{-1} Mpc] results in a 15 per cent difference in bias between scales $s = 3$ [h^{-1} Mpc] and ∞, a value of $s_x = 2$ [h^{-1} Mpc] a 29 per cent difference, etc.

There is a clear pattern illustrated in Fig. 5 of s_x decreasing and then increasing roughly linearly with mass about a pivot point which varies with redshift and ratio type. This is a result of bias effects being suppressed at small scales for small halo masses (i.e. $\mathcal{S} = -1$), passing a point at which there is no scale dependence ($s_x = 0$), and then increasing with enhanced small-scale bias at large values of halo mass (i.e. $\mathcal{S} = +1$). As such, the point of minimum s_x for each case indicates a halo mass at which scale dependence of bias disappears. This behaviour is discernible in Fig. 4.

Motivated by these results, we choose the following parametrization for the halo mass dependence of scale-dependent bias:

$$\begin{aligned} \log_{10} b_x^2(z, V_{max}) &= b_x^0(z) + b_x^V(z) V_{max} \\ s_x(z, V_{max}) &= s_x^V(z) |V_{max} - V_{SF,x}(z)| \\ \mathcal{S}(z, V_{max}) &= \begin{cases} -1 & \text{if } V_{max} < V_{SF,x}, \\ +1 & \text{if } V_{max} \geq V_{SF,x} \end{cases} . \end{aligned} \tag{3}$$

This represents a four-parameter model describing the mass dependence of bias and its scale dependence at a fixed redshift. Two parameters describe a linear V_{max} dependence for the logarithmic bias (b_x^0 and b_x^V), one sets the strength of the mass dependence of scale-dependent bias (s_x^V) and one sets the mass at which bias becomes scale free at the regime between the suppression (at $V_{max} < V_{SF,x}$) and the enhancement of bias at small scales (at $V_{max} > V_{SF,x}$). The results of fitting this model to the cases illustrated in Fig. 5 are

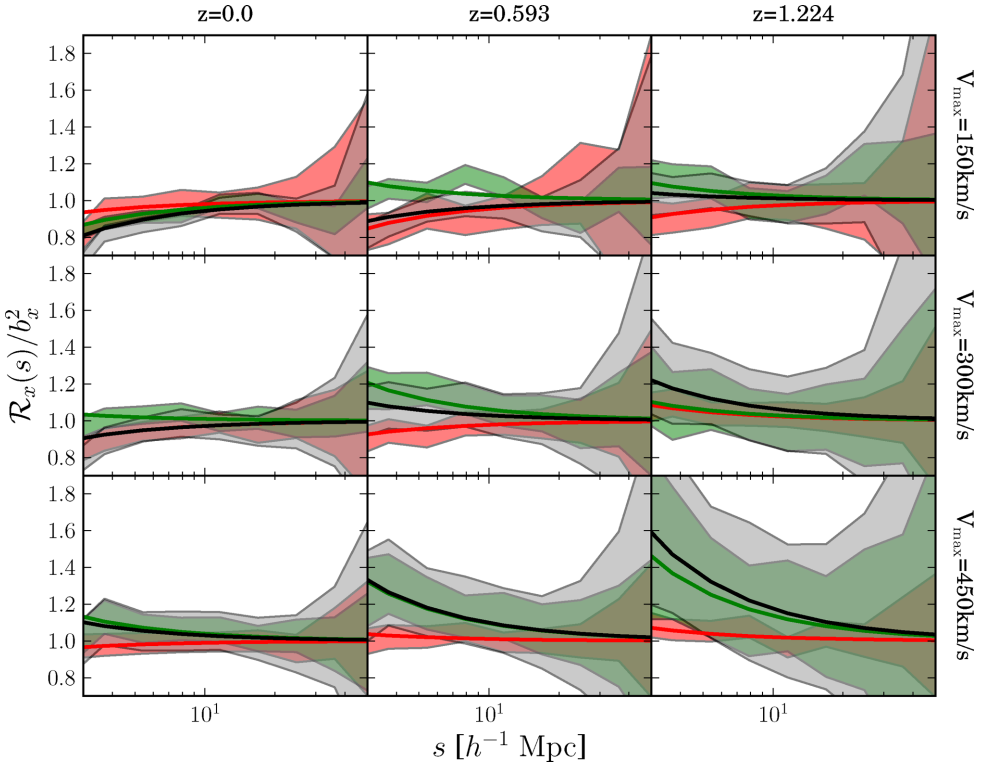

Figure 4. The scale dependence of three ratios taken between total matter and halo correlation functions at the same three halo masses and three redshifts depicted in Fig. 3. Red denotes the ratio of the redshift-space halo correlation function to the real-space halo correlation function ($\mathcal{R}_z$, expressing the square of redshift-space boost effects on the total redshift-space bias), green the ratio of the real-space halo correlation function to the real-space total matter correlation function ($\mathcal{R}_h$, expressing the square of the real-space halo bias) and grey the ratio of the redshift-space halo correlation function to the real-space total matter correlation function ($\mathcal{R}_t$, expressing the square of the total redshift-space bias). All ratios have been computed using their jackknife subsamples to minimize cosmic variance, with shaded regions indicating 68 per cent confidence intervals. Thick solid lines indicate the best fit of equation (2) to each data set assuming $\eta = 1$. In all cases, the square of the large-scale bias (b_x^2) has been normalized-out such that all curves converge to a value of 1 at large values of s. Values across the top denote the redshift represented by each column while values along the right indicate the halo mass (expressed in terms of maximum halo circular velocity, $V_{\rm max}$) represented by each row.

illustrated with solid lines. For this and all cases which follow, these fits are applied directly to the $\mathcal{R}_x$ profiles and their (possibly asymmetric) uncertainty distribution obtained in the manner described in Section 3.1 (and not to the individual points depicted in Fig. 5 resulting from our χ^2 fits to individual cases) using the Markov chain Monte Carlo (MCMC) machinery introduced in Poole et al. (2013).

3.3 The redshift dependence of scale-dependent bias and the final full model

Finally, we now seek a parametrization of the full mass and redshift dependence of scale-dependent bias. This is achieved by parametrizing the redshift dependence of the four parameters in the model given by equation (3) for each ratio type.

In Fig. 6 we present a series of fits (in coloured points) of the model presented in equation (3) at several redshifts spanning the range of our study for both our FoF (solid points) and substructure haloes (open points). Once again, these are preliminary illustrative fits constructed using a simple χ^2-minimization approach and are meant only to motivate the parametrization of our final model. They are equivalent to the fits shown with solid lines in Fig. 5 but applied to a larger number of redshifts (and to both halo types). We find that the parameters of our mass-dependence model vary smoothly with redshift, motivating the following form for the redshift dependence of scale-dependent bias:

$$\begin{aligned}
\log_{10} V_{{\rm SF},x}(z) &= V^0_{{\rm SF},x} + V^{\rm z}_{{\rm SF},x} z \\
s^V_x(z) &= s^{V,0}_x + s^{V,{\rm z}}_x z \\
b^0_x(z) &= \begin{cases} b^{0,0}_x + b^{0,{\rm z}}_x z & \text{if } x = \text{`}h\text{' or `}t\text{'}, \\ b^{0,0}_{\rm z} + b^{0,{\rm zz}}_{\rm z}(z - z_{{\rm b,z}})^2 & \text{if } x = \text{`}z\text{'} \end{cases} \\
b^V_x(z) &= b^{V,0}_x + s^{V,{\rm z}}_x z. \qquad (4)
\end{aligned}$$

This represents a linear redshift dependence for all of the parameters in equation (3) with the exception of the parameters for the Kaiser boost which we find requires a quadratic dependence for $b^0_x(z)$ centred on redshift $z_{\rm b,\,z}$ (hence introducing an extra parameter in this case). Although very-nearly constant with redshift, we find this refined form of redshift dependence is necessary due to the strong dependence of s_x on b_x when $\mathcal{R}_x$ is only weakly scale-dependent (which is always the case for $\mathcal{R}_z$).

Also presented in Fig. 6 (with lines, solid for FoF haloes and dotted for substructure) is the result of our final global MCMC fit to our full data set. This fit is applied simultaneously to all of the $\mathcal{R}_x$ profiles measured for every grouping at all redshifts employed for this study (and not to the plotted points). We find that our chosen parametrization closely follows the individual fits presented with coloured points, validating our assumed form for the redshift

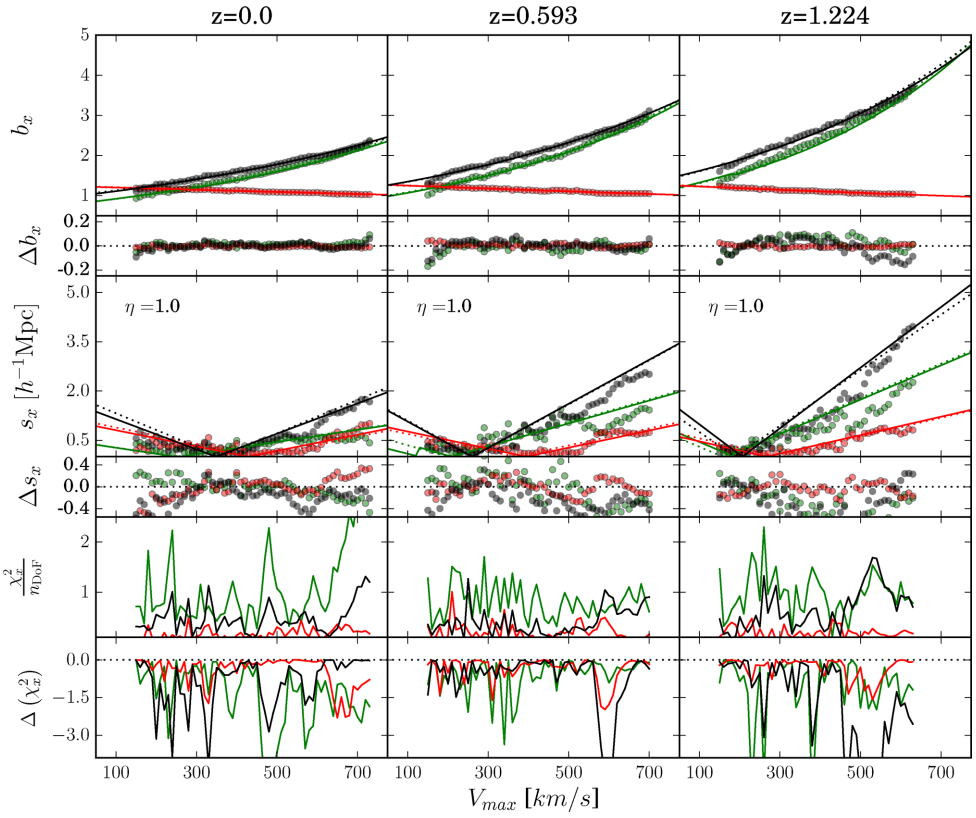

Figure 5. The results of fitting the scale-dependent bias model of equation (2) to halo groupings of various masses (expressed in terms of maximum halo circular velocity, V_{max}) at three redshifts spanning the range utilized in this study. Coloured points indicate fits for redshift-space boost effects ($\mathcal{R}_{\mathrm{z}}$: red), real-space halo bias ($\mathcal{R}_{\mathrm{h}}$: green) and total redshift-space bias ($\mathcal{R}_{\mathrm{t}}$: black). Solid lines indicate the fit of the halo mass dependence model expressed by equation (3) to each of these three data sets (with matching colours). Dotted lines similarly indicate the results of our full mass- and redshift-dependent bias model expressed by equations (2), (13) and (4) and Table 2. Residual differences of each fit from this model are plotted as Δs_x and Δb_x for the large-scale bias and amplitude of scale-dependant bias, respectively. The bottom two panels in each column indicate the values of χ^2/n_{DoF} (where $n_{\mathrm{DoF}} = 6$ in all cases) obtained from the fit assuming $\eta = 1$ (second from bottom) and the difference in χ^2 obtained when allowing η to vary over the range 0–3 (bottom; $n_{\mathrm{DoF}} = 5$ in this case). Values across the top denote the redshift represented by each column.

dependences of each parameter. The resulting parameters describing our full scale-dependent bias model, as described by equations (2) (under the assumption that $\eta = 1$), (3) and (4), are presented in Table 2 for both the FoF and substructure haloes of our simulation.[2] The quality of fit across the whole range of redshifts and masses used to constrain this model is presented in Fig. 7. It is here that the efficacy of our chosen parametrization should be judged and over the vast majority of the probed mass and redshift range, the quality of fit is very good. At the highest masses, the quality of fit declines presumably due to overly coarse mass binning demanded by the limited volume available to us for this study.

3.4 Qualitative trends with mass, redshift and halo type

Several interesting general trends regarding the dependence of bias (and its scale dependence) on mass, redshift and halo type emerge at this point. Commenting first on the halo mass at which bias becomes scale free (V_{SF}), we see that for all bias ratios V_{SF} declines with redshift at a similar rate in all cases and in a nearly identical way for both FoF groups and substructure. This mass scale is higher for Kaiser boost effects however, leading to a significant increase in this mass scale for the total redshift-space results over that from real-space halo bias effects alone. For the full redshift range of our study ($z \lesssim 1.2$), V_{SF} is restricted to the range 150–350[km s^{-1}]. From equation (3) we can see that this trend in $V_{\mathrm{SF}}(z)$ acts to drive an increase in the amplitude of scale-dependent bias (s_x) with redshift at masses above this range (where scale-dependent bias always results in enhanced bias at small scales) and a suppression of its amplitude on mass scales below it (where scale-dependent bias always results in suppressed bias at small scales).

Augmenting these trends in s_x driven by the evolution of $V_{\mathrm{SF}}(z)$, the mass dependence of s_x (given by s_x^V) also increases with redshift. Interestingly, this is the only parameter for which redshift-space contributions to total bias differ between FoF and substructure haloes: being significantly higher for substructure, driving an enhanced mass dependence in the total redshift-space bias as well.

We now focus on our results for large-scale bias (b_x). In Fig. 8 we illustrate this quantity for all of our groupings at three redshifts spanning the range of our study. In this case, we directly compare results for FoF (solid points) and substructure haloes (open points). In this figure we also compare our results to the successful simulation-calibrated excursion set model of TRK (dashed green lines), the redshift-space distortion model of K87 (dashed red) and the redshift-space model that emerges from combining the two (dashed black). The K87 model predicts a redshift-space boost given

[2] A PYTHON script with the full model and its coefficients has been made available online at http://gbpoole.github.io/Poole_2014a_code/

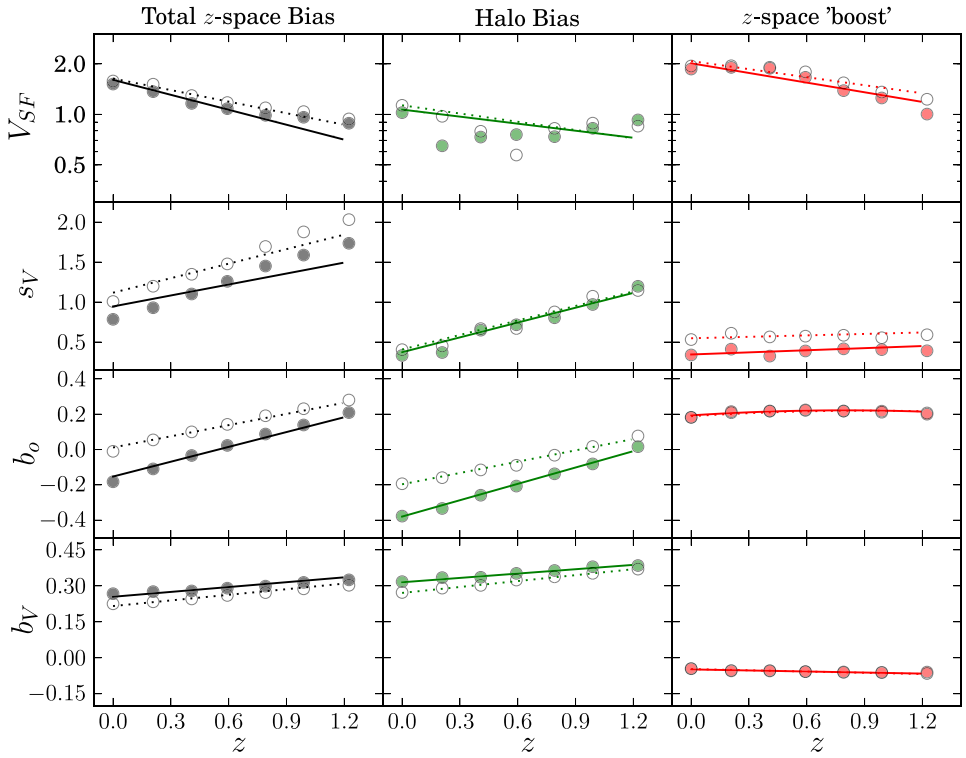

Figure 6. The results of fitting our final redshift-and-mass dependent model to the profiles of redshift-space boost effects, real-space halo bias and total z-space bias computed for this study. Individual points denote fits of equation (3) to $\mathcal{R}_x(s, V_{\rm max})$ for each ratio type at several redshifts with solid points indicating fits to FoF haloes and open points indicating fits to substructure haloes. Solid lines denote our full mass- and redshift-dependent model expressed by equation (4) when fit to FoF haloes and dashed lines denote this fit to substructure haloes. Note that the solid lines are not fits to the data points, but rather a single joint MCMC fit to all $\mathcal{R}_x(s)$ profiles used in this study. The agreement validates our chosen parametrization of the redshift dependence of the parameters in our final model.

Table 2. Parameters for our full scale-dependent bias model, as expressed by equations (2), (3) and (4). Values for both halo types (FoF haloes and substructure) are given.

Parameter	Real-space bias		z-space boost		Total z-space bias	
	FoF haloes	Substructure	FoF haloes	Substructure	FoF haloes	Substructure
$V^{0}_{{\rm SF},x}$ [220 km s^{-1}]	0.028 19	0.053 26	0.310 02	0.317 31	0.204 17	0.212 87
$V^{z}_{{\rm SF},x}$ [220 km s^{-1}]	−0.138 20	−0.167 39	−0.202 64	−0.159 91	−0.296 67	−0.228 06
$s_x^{V,0}$ [(220 km s^{-1})$^{-1}$]	0.368 60	0.402 69	0.334 23	0.534 44	0.940 82	1.118 79
$s_x^{V,z}$ [(220 km s^{-1})$^{-1}$]	0.615 47	0.609 66	0.092 33	0.071 02	0.451 47	0.612 14
$b_x^{0,0}$	−0.379 36	−0.197 43	0.220 62	0.219 88	−0.153 50	0.011 98
$b_x^{0,z}$	0.307 43	0.213 82	n/a	n/a	0.279 95	0.211 27
$b_x^{0,zz}$	n/a	n/a	−0.044 19	−0.037 49	n/a	n/a
$z_{{\rm b},z}$	n/a	n/a	0.785 27	0.929 20	n/a	n/a
$b_x^{V,0}$ [(220 km s^{-1})$^{-1}$]	0.314 75	0.270 75	−0.048 05	−0.046 29	0.254 71	0.215 35
$b_x^{V,z}$ [(220 km s^{-1})$^{-1}$]	0.060 73	0.082 02	−0.014 54	−0.018 33	0.067 61	0.077 63

by (his equation 3.8, cast here in terms of our notation)

$$b_z^2 = 1 + \frac{2}{3}\beta + \frac{1}{5}\beta^2, \tag{5}$$

where $\beta = f/b_{\rm h}$ with f being the logarithmic derivative of the linear growth factor with respect to expansion factor given by

$$f = \frac{{\rm d}\ln D}{{\rm d}\ln a}. \tag{6}$$

Lastly, we also combine the TRK and K87 models to produce a reference total redshift-space bias model (dashed black lines).

Over most of the range of masses and redshifts probed by our study, we find very good agreement between these reference models and our FoF large-scale bias results. Since the FoF catalogues most straightforwardly relate to the density structures described by excursion set models, this is as expected. At the highest masses and redshifts, there is a tendency for the TRK model to predict higher real-space biases than our model predicts. It is possible that the calibration of the TRK model has been biased high from the very strong scale-dependant bias of haloes in this regime, but this is difficult to discern since their study is conducted in Fourier space and since it is unclear from the presentation of their analysis what exact scale they have fit to.

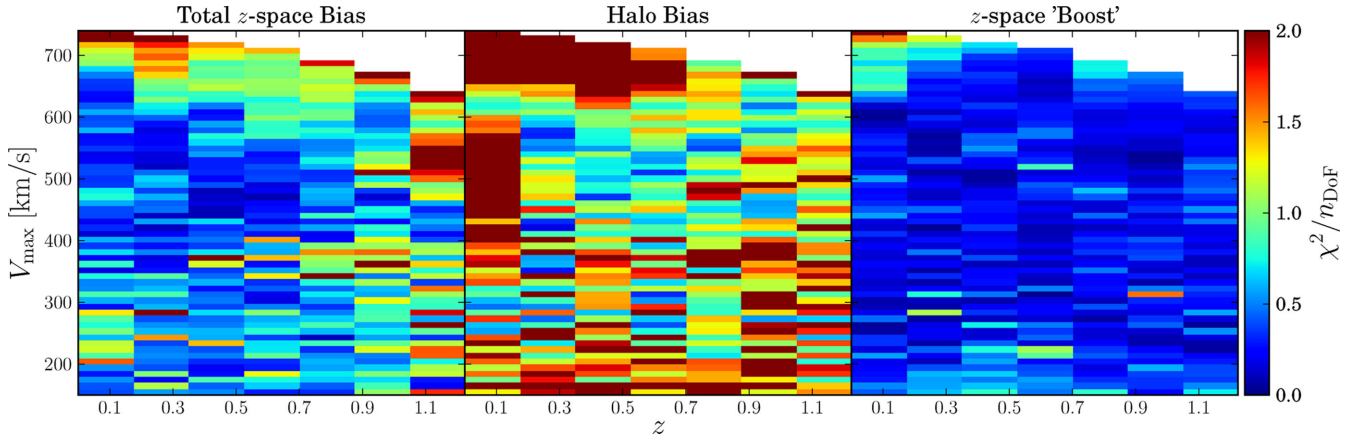

Figure 7. Values of $\chi^2/n_{\rm DoF}$ (where $n_{\rm DoF} = 6$ in all cases) obtained from fitting our scale-dependent bias model – $b_{\rm t}(V_{\rm max}, z)$ on the left, $b_{\rm h}(V_{\rm max}, z)$ in the middle, $b_{\rm z}(V_{\rm max}, z)$ on the right – to the FoF haloes of the GiggleZ-main simulation. These planes represent the full range in $V_{\rm max}$ and z over which our model has been constrained, with the white region in the top right being due to a lack of dark matter haloes of sufficient density at corresponding masses and redshifts.

Additionally, looking at substructure we find significant enhancements in our large-scale real-space (and by extension, total redshift-space) halo biases at low redshift. This difference is approximately 20 per cent for Milky Way-sized systems ($\sim$220 km s^{-1}) at redshift zero and increases with declining mass.

Interestingly (but perhaps not unexpected), there is absolutely no difference between the two halo populations in terms of their Kaiser boosts. We interpret this similarity as a reflection of the fact that non-linear pairwise velocities are unimportant on the largest scales of our study. Furthermore, there is extremely little redshift dependence and only a slight mass dependence for $b_{\rm z}$. We see excellent agreement with the K87 model and interpret the lack of evolution in the Kaiser boost as a remarkable cancelling of the effects on β from evolution in the growth of structure (via evolution in f) and in real-space halo bias (via evolution in $b_{\rm h}$). We note that this level of agreement with the K87 model was also found by Montesano et al. (2010, see their table 4) in their Fourier-space study of bias.

4 SYSTEMATIC BIASES IN GROWTH OF STRUCTURE MEASUREMENTS

Having developed our full parametrization of scale-dependant bias, we seek now to quantify the systematic bias that results in growth of structure measurements when the scale dependence of bias is not taken into account. This is done by applying an extension of the Fisher matrix formalism to our bias model in Fourier space where covariance is minimized and measurement uncertainties are more straightforwardly modelled. We intend for this to be an illustration of the effects of scale-dependant bias on measurements of this sort and caution that our estimates here may be somewhat pessimistic. This is because we will assume a specific and fixed redshift-space distortion model for this calculation whereas fits to data usually marginalize over a velocity-dispersion parameter ($\sigma_{\rm v}$) which can absorb some of the systematic we present here. Nevertheless, we expect the general trends and effects presented here to be an informative illustration of the circumstances in which systematic bias should be taken into account in growth of structure studies.

4.1 Estimation of systematic bias

To express our bias model in Fourier space, we first compute an unbiased 2D power spectrum ($P(k, \mu)$, where $\mu = \cos(\theta)$ with θ being the angle between the Fourier mode and the line-of-sight) by applying the K87 redshift-space distortion model to a 1D CAMB power spectrum:

$$P_{\rm model}(k, \mu) = (b_{\rm h} + f\mu^2)^2 P_{\rm CAMB}(k). \quad (7)$$

We then convert this 2D Fourier space model to configuration space using equation (11) of Reid et al. (2012, see also Hamilton 1998) which relates correlation function multipoles (indexed by ℓ) to those of its associated power spectrum:

$$\xi_\ell(s) = \frac{i^\ell}{2\pi^2} \int P_\ell(k) j_\ell(ks) k^2 \, {\rm d}k, \quad (8)$$

and apply our bias model to the result. This is done for both our scale-dependent bias model and a constant bias model, yielding (once we convert back to Fourier space) the biased power spectra $P_{\rm model}(k, \mu)$ and $P_{\rm sys}(k, \mu)$, respectively.

For our estimation of systematic bias in f (which we denote by $\Delta f_{\rm b}$), we follow the method of Amara & Réfrégier (2008). This method employs a straightforward extension of the Fisher matrix formalism with the adjustment that uncertainties from systematic biases in parameters are separated explicitly from statistical uncertainties (rather than treated, for example, as an additive term to the statistical contribution to be marginalized over). Defining the Fisher matrix in the usual way for a 2D power spectrum dependant on a set of parameters $p_i = \{f, ...\}$ with covariance C_{ij} between each (k, μ) power spectrum bin as

$$\mathbf{F}_{ij} = \sum_{(k,\mu)} C_{ij}^{-2} \frac{{\rm d}P_{\rm model}(k, \mu, p)}{{\rm d}p_i} \frac{{\rm d}P_{\rm model}(k, \mu, p)}{{\rm d}p_j}, \quad (9)$$

the systematic uncertainty in each parameter (which we denote generically as Δp_i) is obtained by projecting the inverse of this Fisher matrix along a bias vector $\boldsymbol{B}_j$ as given by the expression

$$\Delta p_i = \mathbf{F}_{ij}^{-1} \boldsymbol{B}_j. \quad (10)$$

For the parameter $p_0 = f$, the relevant expression for B_0 is found by rewriting equation (8) of Amara & Réfrégier (2008) in the following form:

$$B_0 = \sum_{(k,\mu)} \frac{\Delta P_{\rm sys}(k, \mu, f)}{\sigma_P^2(k, \mu)} \frac{{\rm d}P_{\rm model}}{{\rm d}f}(k, \mu, f), \quad (11)$$

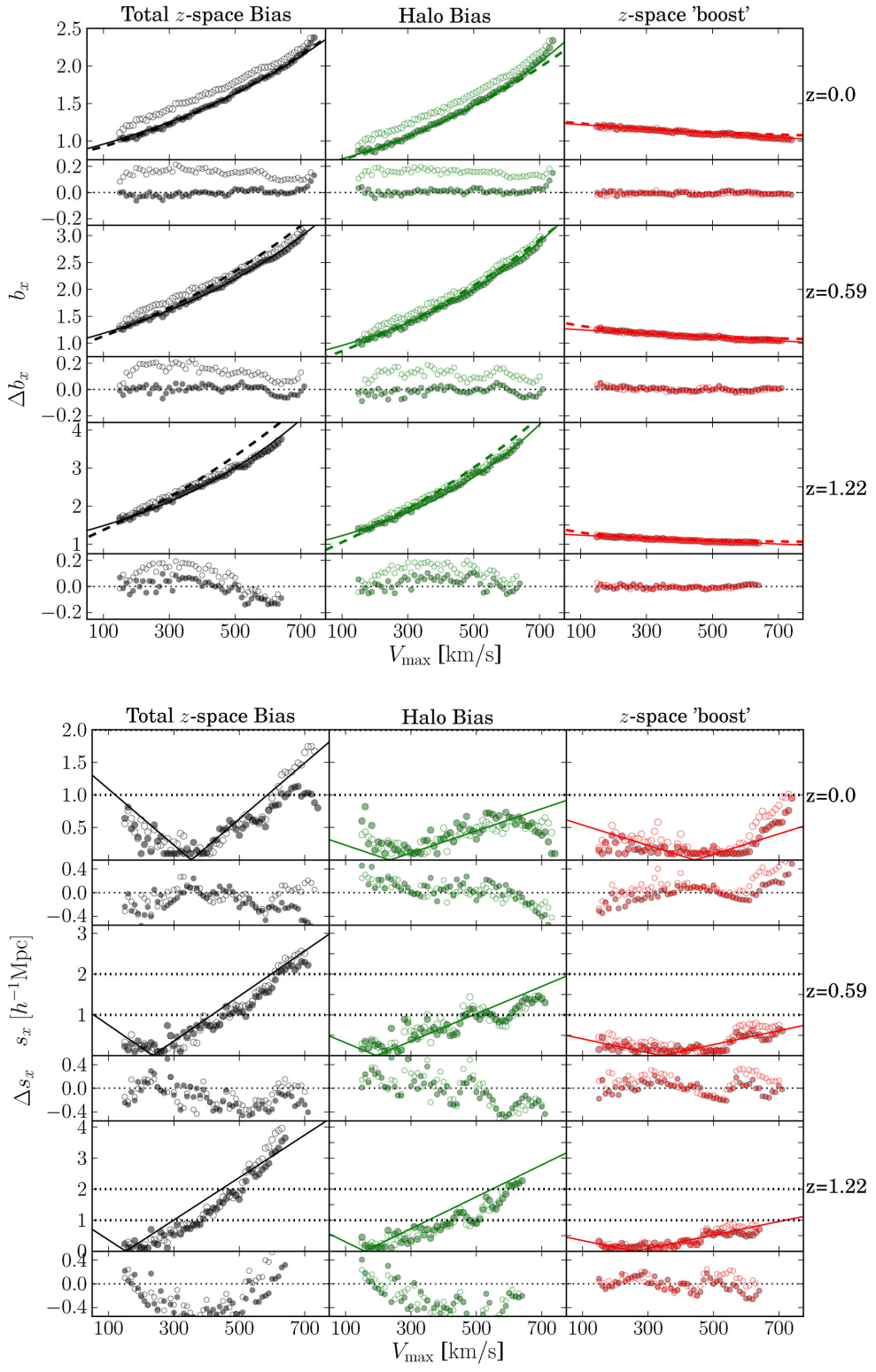

Figure 8. Plots comparing the large-scale bias (top) and amplitude of the scale dependence of bias (bottom) of FoF haloes (solid points) and substructure haloes (open points) in the GiggleZ-main simulation. Solid lines show our final bias model and dashed lines show the simulation-calibrated excursion set model of TRK (dashed green), the redshift-space boost model of K87 (dashed red) and the total z-space bias resulting from both (dashed black). Residual differences of each fit from our final global model for the case of FoF haloes are plotted as Δs_x and Δb_x for the large-scale bias and amplitude of scale-dependant bias, respectively. Horizontal dotted lines in the right-hand panel denote the values of s_x which yield differences in bias between scales s =3 [h^{-1} Mpc] and ∞ of 15 per cent ($s_x = 1$ [h^{-1} Mpc]) and 30 per cent ($s_x = 2$ [h^{-1} Mpc]).

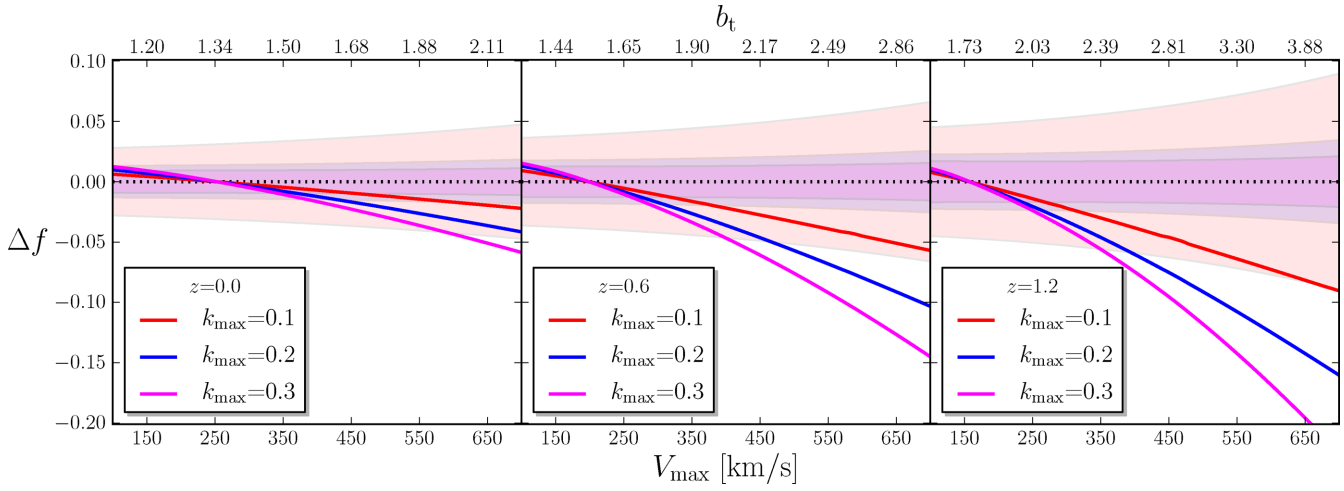

Figure 9. The systematic bias induced in measurements of the growth rate of cosmic structure (Δf) due to an incorrect assumption of constant galaxy bias (Δf_b; solid lines) for several cut-off measurement scales (k_{max}; for values 0.1, 0.2, 0.3 $[h^{-1}\,\mathrm{Mpc}]^{-1}$ in red, blue and magenta, respectively) compared to the statistical uncertainty in this measurement (Δf_s) for a fiducial survey with volume 1 $[h^{-1}\,\mathrm{Gpc}]^3$ and number density 3×10^5 $[h^{-1}\,\mathrm{Gpc}]^{-3}$ (shaded regions: pink, blue and magenta for k_{max} =0.1, 0.2, 0.3 $[h^{-1}\,\mathrm{Mpc}]^{-1}$, respectively).

with $\sigma_P(k, \mu)$ being the error in each 2D power spectrum bin given by

$$\sigma_P(k, \mu) = \frac{P(k, \mu) + 1/n}{\sqrt{N}}, \tag{12}$$

with n being the number density of galaxies and N the number of Fourier modes in each bin. The quantity $\Delta P_{sys} = P_{model} - P_{sys}$ represents the residual systematic modelling error in the power spectrum. Lastly, $\mathrm{d}P_{model}/\mathrm{d}f$ gives the partial derivative of our model power spectrum with respect to f. Throughout, we use bin widths of $\Delta k = 0.01$ $[h^{-1}\,\mathrm{Mpc}]^{-1}$ and $\Delta\mu = 0.1$ for sums over k and μ, respectively.

4.2 Effects of systematic bias

To evaluate the magnitude of this systematic bias, we express it here for a fiducial survey of volume 1 $[h^{-1}\,\mathrm{Gpc}]^3$ and number density $n = 3 \times 10^5$ $[h^{-1}\,\mathrm{Gpc}]^{-3}$. This number density is chosen to be similar to that of both the WiggleZ and BOSS (The Baryon Oscillation Spectroscopic Survey) surveys and the volume is representative of current large spectroscopic surveys. In Fig. 9, we show the results of this calculation at three redshifts spanning the range $z \lesssim 1.2$ for three small-scale cut-offs (denoted k_{max}). These are compared in each case to the statistical uncertainty expected for this measurement (denoted Δf_s; shown with shaded regions) which we calculate using a standard Fisher matrix forecast (see White, Song & Percival 2009; Abramo et al. 2012; Blake et al. 2013) using the same binning and range as for the systematics forecast.

Noting first some generic trends in this figure, we see that Δf_b is positive for low masses/biases and (more generally) negative for larger masses/biases. This is due to the transition from $\mathcal{S} = -1$ (suppression of bias on small scales) to $\mathcal{S} = +1$ (enhancement of bias on small scales) with suppressed small-scale bias leading to a positive bias in f and enhanced small-scale bias (the more common case) leading to a negative bias in f. Additionally, we see that increasing k_{max} has two distinct effects: it increases the precision of the measurement (particularly between k_{max}=0.1 and 0.2 $[h^{-1}\,\mathrm{Mpc}]^{-1}$) due to the additional data involved and it increases Δf_b due to the use of scales where scale-dependent bias has an increased effect on the shape of the power spectrum.

Commenting more specifically, we can see from this figure that when $k_{max} = 0.1$ $[h^{-1}\,\mathrm{Mpc}]^{-1}$, Δf_b remains significantly smaller than Δf_s for all cases with $b_t \lesssim 2$. Indeed, only when $b_t \gtrsim 3$ at $z \gtrsim 1$ does the systematic bias become significant compared to the precision of the measurement. However, this situation dramatically changes for larger values of k_{max}. When it increases to 0.2, Δf_b becomes significant compared to Δf_s for all cases except those very narrowly similar in mass to V_{SF}, where scale-dependent bias disappears.

The presentation of these results is expanded in Fig. 10 where we show Δf_b for the full range of cases to which our bias model has been constrained. Across all redshifts and for all cases, we see that scale-dependant bias effects are minimized when the halo population has a bias similar to $b_t \sim 1.5$.

5 SUMMARY AND CONCLUSIONS

We have used the GiggleZ-main simulation to produce an eight-parameter phenomenological model quantifying halo bias (in both real and redshift spaces) and its scale dependence over the range of masses $100[\mathrm{km\,s^{-1}}] < V_{max} < 700[\mathrm{km\,s^{-1}}]$, redshifts $z \lesssim 1.2$ and scales $3[\mathrm{Mpc}\,h^{-1}] < s < 100[\mathrm{Mpc}\,h^{-1}]$ under the ansatz that bias converges to a scale-independent form at large scales. We find that scale-dependent bias can either enhance or suppress bias at small scales. For any given halo mass at any given redshift, large-scale bias is given by a single constant and the scale dependence of bias is given by two others: a binary parameter determining whether bias is enhanced or supressed on small scales ($\mathcal{S}$) and a parameter setting its amplitude (s).

While a relatively small but growing body of literature has looked at scale-dependent bias effects in the Fourier domain, few recent studies have addressed it in configuration space. The results presented in this work should not only be more directly applicable to observational studies conducted in configuration space, but should also help provide a basis upon which to build some intuition regarding the scale-dependent bias effects observed in Fourier-space studies.

We find several interesting trends (noted and discussed in Section 3.4) which require further study to understand. Most prominent among these is the fact that scale dependence of bias transitions from

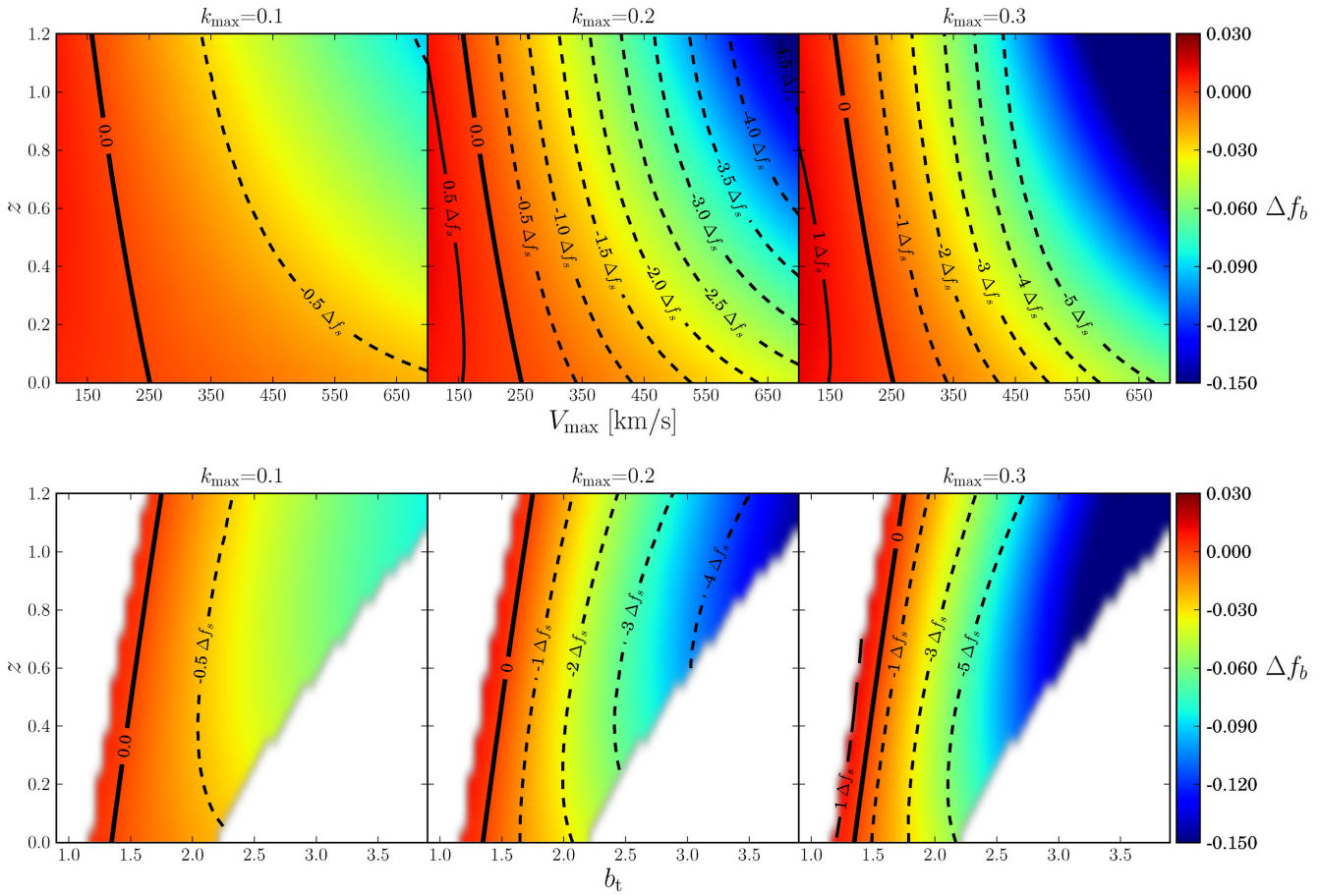

Figure 10. The systematic bias induced in measurements of the growth rate of cosmic structure (Δf_b) due to an incorrect assumption of constant galaxy bias for several measurement scale cut-offs (k_{max}; values given in text above each panel) as a function of redshift and halo mass (quantified by maximum circular velocity, V_{max}; top) or total redshift-space bias (b_t; bottom). Black contours express this in units of the statistical uncertainty in this measurement (Δf_s; dashed contours for negative systematic biases, solid lines for positive systematic biases) for a fiducial survey with volume 1 $[h^{-1}\,\mathrm{Gpc}]^3$ and number density 3×10^5 $[h^{-1}\,\mathrm{Gpc}]^{-3}$. Thick solid contours indicate the cases where scale-dependent bias vanishes on scales larger than 3 $[h^{-1}\mathrm{Mpc}]$ resulting in no systematic bias in f.

the suppression of bias at small scales for small masses to enhancement for large masses. It does so in a narrow bias range centred on $b_t \sim 1.5$ across all redshifts $z \lesssim 1.2$. At the transition between, our parametrization describes bias as scale free. It is important to note however, that while a scale-free model is a good fit in these regimes, the claim of a scale-free bias can only be made to a precision allowed by our simulation. Additionally, we wish to emphasize that the functional form of our parametrization as well as the specific parameter values we have obtained may need to vary under reasonable changes from our fiducial cosmology. Further study is needed to determine how sensitively they do so.

It should also be noted that we restrict our study to configuration space on scales larger than 3[Mpc h^{-1}]. On scales lower than this, a wide variety of non-monotonic variations in $\mathcal{R}_x$ occur (of a character similar to that presented in fig. 4 of Zehavi et al. 2004). In the Fourier domain, these features are likely to have broad spectral content and more detailed study is required to understand their influence in Fourier space.

Lastly, we compute the systematic biases induced in growth of structure measurements in the absence of corrections for scale-dependent bias effects. We find that for a fiducial survey with volume 1 $[h^{-1}\,\mathrm{Gpc}]^3$ and number density $n = 3 \times 10^5$ $[h^{-1}\,\mathrm{Gpc}]^{-3}$ that systematic bias is modest when scales only as small as $k_{max} = 0.1$ are used, except for highly biased haloes at high redshift. Once scales as short as $k_{max} \gtrsim 0.2$ are utilized, the situation dramatically changes with significant systematic biases resulting at all redshifts for biases even just slightly different from $b_t \sim 1.5$. In realistic analysis where fits are generally marginalized over a pair-wise velocity dispersion parameter, much of this effect is likely to be absorbed into this parameter, reducing the problem at the expense of compromising any meaning given to this quantity. Further study under realistic conditions is clearly needed to precisely quantify these effects on real survey results.

These results suggest that the optimal strategy at all redshifts $z \lesssim 1.2$ for clustering studies which are dominated more by systematic effects than statistical precision (such as the case of cosmological neutrino mass measurements) is to target $b_t \sim 1.5$ systems. Fortuitously, the UV-selected galaxies targeted by the WiggleZ survey have a large-scale bias similar to this (Blake et al. 2009), for example.

These results reenforce the notion that scale-dependent bias is particularly significant for studies involving measurements of the *shape* of two-point clustering statistics. We have focused here on growth of structure measurements only, but similar analysis

(following-on from the work of Swanson, Percival & Lahav 2010, for example) for neutrino mass measurements are clearly warranted as well.

Of course, this study has focused on the bias properties of halo tracers with complete selection properties and uniform masses. The larger bias we find for substructure catalogues shows the importance of realistically considering the sites of galaxy formation. We now need to carefully consider the effects that can be induced by the sorts of colour selections employed during observational campaigns. Due to phenomena like the morphology–density relation, a large variety of differing results can occur if galaxies are selected by more observationally motivated criteria (e.g. luminosity or colour) which are more difficult to robustly model. A great deal more study on these issues is required to make robust statements under such circumstances.

ACKNOWLEDGEMENTS

We would like to thank Volker Springel for making GADGET-2 publicly available and for permitting us to use his halo-finding code (SUBFIND) and Aaron Ludlow for useful comments. We would also like to thank Swinburne University for its generous allocation of computing time (on the Green and gSTAR facilities) for this project, Jarrod Hurley and the Green Machine Help Desk for their computing support, and the Green Machine user community for patiently waiting while the GiggleZ-main simulation kept them from their work. We acknowledge financial support from the Australian Research Council through Discovery Project grants DP0772084 and DP1093738. GBP and SJM acknowledge support from the ARC Laureate programme of Stuart Wyithe. CB and CP acknowledge the support of the Australian Research Council through the award of a Future Fellowship. DJC acknowledges the support of an Australian Research Council QEII Fellowship.

REFERENCES

Abramo L. R. et al., 2012, MNRAS, 423, 3251
Amara A., Réfrégier A., 2008, MNRAS, 391, 228
Angulo R. E., Baugh C. M., Frenk C. S., Lacey C. G., 2008, MNRAS, 383, 755
Angulo R. E., White S. D. M., Springel V., Henriques B., 2014, MNRAS, 442, 2131
Bahé Y. M., McCarthy I. G., Balogh M. L., Font A. S., 2013, MNRAS, 430, 3017
Bardeen J. M., Bond J. R., Kaiser N., Szalay A. S., 1986, ApJ, 304, 15
Barkana R., Loeb A., 2011, MNRAS, 415, 3113
Basilakos S., Plionis M., 2001, ApJ, 550, 522
Basilakos S., Plionis M., Ragone-Figueroa C., 2008, ApJ, 678, 627
Baugh C. M., 2013, PASA, 30, 30
Bertschinger E., 2001, ApJS, 137, 1
Blake C. et al., 2009, MNRAS, 395, 240
Blake C. et al., 2011a, MNRAS, 415, 2876
Blake C. et al., 2011b, MNRAS, 415, 2892
Blake C. et al., 2013, MNRAS, 436, 3089
Blake C., James J. B., Poole G. B., 2014, MNRAS, 437, 2488
Borzyszkowski M., Ludlow A. D., Porciani C., 2014, MNRAS, 445, 4124
Buchert T., 1992, MNRAS, 254, 729
Casas-Miranda R., Mo H. J., Sheth R. K., Boerner G., 2002, MNRAS, 333, 730
Cole S. et al., 2005, MNRAS, 362, 505
Coles P., Erdogdu P., 2007, J. Cosmol. Astropart. Phys., 10, 007
Contreras C., Blake C., Poole G. B., Marin F., 2013, MNRAS, 430, 934
Cresswell J. G., Percival W. J., 2009, MNRAS, 392, 682
Crocce M., Scoccimarro R., 2008, Phys. Rev. D, 77, 23533
Crocce M., Pueblas S., Scoccimarro R., 2006, MNRAS, 373, 369
Dalal N., Doré O., Huterer D., Shirokov A., 2008, Phys. Rev. D, 77, 123514
Drinkwater M. J. et al., 2010, MNRAS, 401, 1429
Eisenstein D. J., Seo H.-J., White M., 2007, ApJ, 664, 660
Elia A., Ludlow A. D., Porciani C., 2012, MNRAS, 421, 3472
Guzik J., Bernstein G., Smith R. E., 2007, MNRAS, 375, 1329
Haines C. P. et al., 2009, ApJ, 704, 126
Hamilton A. J. S., 1998, Astrophys. Space Sci. Libr., 231, 185
Hansen S. M., Sheldon E. S., Wechsler R. H., Koester B. P., 2009, ApJ, 699, 1333
Hermit S., Santiago B. X., Lahav O., Strauss M. A., Davis M., Dressler A., Huchra J. P., 1996, MNRAS, 283, 709
Huff E., Schulz A. E., White M., Schlegel D. J., Warren M. S., 2007, Astropart. Phys., 26, 351
Jennings E., Baugh C. M., Pascoli S., 2011, ApJ, 727, L9
Jing Y. P., 1998, ApJ, 503, L9
Jing Y. P., 1999, ApJ, 515, L45
Kaiser N., 1984, ApJ, 284, L9
Kaiser N., 1987, MNRAS, 227, 1 (K87)
Komatsu E. et al., 2009, ApJS, 180, 330
Landy S. D., Szalay A. S., 1993, ApJ, 412, 64
Lewis A., Challinor A., Lasenby A., 2000, ApJ, 538, 473
Loveday J., Maddox S. J., Efstathiou G., Peterson B. A., 1995, ApJ, 442, 457
Lu T., Gilbank D. G., McGee S. L., Balogh M. L., Gallagher S., 2012, MNRAS, 420, 126
Ludlow A. D., Porciani C., 2011, MNRAS, 413, 1961
Lukić Z., Heitmann K., Habib S., Bashinsky S., Ricker P. M., 2007, ApJ, 671, 1160
Ma C.-P., Maggiore M., Riotto A., Zhang J., 2011, MNRAS, 411, 2644
Marín F. A. et al., 2013, MNRAS, 432, 2654
Mo H. J., White S. D. M., 1996, MNRAS, 282, 347 (MW)
Montesano F., Sánchez A. G., Phleps S., 2010, MNRAS, 408, 2397
Muñoz-Cuartas J. C., Macciò A. V., Gottlöber S., Dutton A. A., 2011, MNRAS, 411, 584
Navarro J. F., Frenk C. S., White S. D. M., 1997, ApJ, 490, 493
Norberg P. et al., 2001, MNRAS, 328, 64
Okumura T., Jing Y. P., 2011, ApJ, 726, 5
Padmanabhan N. et al., 2007, MNRAS, 378, 852
Papageorgiou A., Plionis M., Basilakos S., Ragone-Figueroa C., 2012, MNRAS, 422, 106
Paranjape A., Sefusatti E., Chan K. C., Desjacques V., Monaco P., Sheth R. K., 2013, MNRAS, 436, 449
Pollack J. E., Smith R. E., Porciani C., 2014, MNRAS, 440, 555
Poole G. B. et al., 2013, MNRAS, 429, 1902
Porciani C., Catelan P., Lacey C., 1999, ApJ, 513, L99
Prada F., Klypin A. A., Cuesta A. J., Betancort-Rijo J. E., Primack J., 2012, MNRAS, 423, 3018
Press W. H., Schechter P., 1974, ApJ, 187, 425
Rasmussen J., Mulchaey J. S., Bai L., Ponman T. J., Raychaudhury S., Dariush A., 2012, ApJ, 757, 122
Reddick R. M., Wechsler R. H., Tinker J. L., Behroozi P. S., 2013, ApJ, 771, 30
Reid B. A. et al., 2012, MNRAS, 426, 2719
Riemer-Sørensen S. et al., 2012, Phys. Rev. D, 85, 81101
Ross A. J., Brunner R. J., Myers A. D., 2007, ApJ, 665, 67
Schulz A. E., White M., 2006, Astropart. Phys., 25, 172
Scoccimarro R., 1998, MNRAS, 299, 1097
Seljak U., 2001, MNRAS, 325, 1359
Seljak U., Warren M. S., 2004, MNRAS, 355, 129
Seo H.-J., Eisenstein D. J., 2005, ApJ, 633, 575
Sheth R. K., Lemson G., 1999, MNRAS, 304, 767
Sheth R. K., Tormen G., 1999, MNRAS, 308, 119
Sheth R. K., Mo H. J., Tormen G., 2001, MNRAS, 323, 1 (SMT)
Slosar A., Hirata C., Seljak U., Ho S., Padmanabhan N., 2008, J. Cosmol. Astropart. Phys., 08, 031
Smith R. E., Scoccimarro R., Sheth R. K., 2007, Phys. Rev. D, 75, 63512
Smith R. E., Scoccimarro R., Sheth R. K., 2008, Phys. Rev. D, 77, 43525

Springel V., 2005, MNRAS, 364, 1105
Springel V., White S. D. M., Tormen G., Kauffmann G., 2001, MNRAS, 328, 726
Swanson M. E. C., Tegmark M., Blanton M., Zehavi I., 2008, MNRAS, 385, 1635
Swanson M. E. C., Percival W. J., Lahav O., 2010, MNRAS, 409, 1100
Taruya A., Koyama K., Matsubara T., 2008, Phys. Rev. D, 78, 123534
Tinker J. L., Weinberg D. H., Zheng Z., Zehavi I., 2005, ApJ, 631, 41
Tinker J. L., Robertson B. E., Kravtsov A. V., Klypin A., Warren M. S., Yepes G., Gottlöber S., 2010, ApJ, 724, 878 (TRK)
von der Linden A., Wild V., Kauffmann G., White S. D. M., Weinmann S., 2010, MNRAS, 404, 1231
Wetzel A. R., Tinker J. L., Conroy C., 2012, MNRAS, 424, 232
White S. D. M., 1994, preprint (arXiv:e-prints)
White M., Song Y.-S., Percival W. J., 2009, MNRAS, 397, 1348
Zehavi I. et al., 2004, ApJ, 608, 16
Zehavi I. et al., 2005, ApJ, 630, 1
Zel'Dovich Y. B., 1970, A&A, 5, 84

SUPPORTING INFORMATION

Additional Supporting Information may be found in the online version of this article:

bias_Poole2014a.py (http://mnras.oxfordjournals.org/lookup/suppl/doi:10.1093/mnras/stv314/-/DC1)

Please note: Oxford University Press is not responsible for the content or functionality of any supporting materials supplied by the authors. Any queries (other than missing material) should be directed to the corresponding author for the article.

This paper has been typeset from a TEX/LATEX file prepared by the author.